

Investigating multi-frequency pulse profiles of PSRs B0329+54 and B1642–03 in an inverse Compton scattering (ICS) model

L. H. Shang^{1,2}, J. G. Lu^{3,4}, Y. J. Du⁵, L. F. Hao⁶, D. Li², K. J. Lee⁷, Bin Li^{8,9}, L. X. Li⁷, G. J. Qiao^{3*}, Z. Q. Shen^{8,9}, D. H. Wang¹, M. Wang⁶, X. J. Wu³, Y. J. Wu^{8,9}, R. X. Xu^{3,4,7}, Y. L. Yue², Z. Yan^{8,9}, Q. J. Zhi^{1†}, R. B. Zhao^{8,9}, R. S. Zhao^{8,9}

¹*School of Physics and Electronic Science, Guizhou Normal University, No. 116, Baoshan Road, Yunyan Distric, Guiyang 550001, China*

²*National Astronomical Observatories, Chinese Academy of Sciences, 20A Datum Road, Chaoyang District, Beijing 100012, China*

³*School of Physics, Peking University, No. 5, Yiheyuan Road, Haidian District, Beijing 100871, China*

⁴*State Key Laboratory of Nuclear Science and Technology, Peking University, No. 5, Yiheyuan Road, Haidian District, Beijing 100871, China*

⁵*Qian Xuesen Laboratory of Space Technology, NO. 104, Youyi Road, Haidian District, Beijing 100094, China*

⁶*Yunnan Astronomical Observatory, Chinese Academy of Sciences, No. 396, Yangfangwang, Guandu District, Kunming 650011, China*

⁷*Kavil Institute for Astronomy and Astrophysics, Peking University, No. 5, Yiheyuan Road, Haidian District, Beijing 100871, China*

⁸*Shanghai Astronomical Observatory, Chinese Academy of Sciences, No. 80, Nandan road, Shanghai 200030, China*

⁹*Key Laboratory of Radio Astronomy, Chinese Academy of Sciences, No. 80, Nandan road, Shanghai 200030, China*

Accepted XXX. Received YYY; in original form ZZZ

ABSTRACT

The emission geometries, e.g. the emission region height, the beam shape, and radius-to-frequency mapping, are important predictions of pulsar radiation model. The multi-band radio observations carry such valuable information. In this paper, we study two bright pulsars, (PSRs B0329+54 and B1642–03) and observe them in high frequency (2.5 GHz, 5 GHz, and 8 GHz). The newly acquired data together with historical archive provide an atlas of multi-frequency profiles spanning from 100 MHz to 10 GHz. We study the frequency evolution of pulse profiles and the radiation regions with the these data. We firstly fit the pulse profiles with Gaussian functions to determine the phase of each component, and then calculate the radiation altitudes of different emission components and the radiation regions. We find that the inverse Compton scattering (ICS) model can reproduce the radiation geometry of these two pulsars. But for PSR B0329+54 the radiation can be generated in either annular gap (AG) or core gap (CG), while the radiation of PSR B1642–03 can only be generated in the CG. This difference is caused by the inclination angle and the impact angle of these two pulsars. The relation of beaming angle (the angle between the radiation direction and the magnetic axis) and the radiation altitudes versus frequency is also presented by modelling the beam-frequency evolution in the ICS model. The multi-band pulse profiles of these two pulsars can be described well by the ICS model combined with the CG and AG.

Key words: stars: neutron – pulsars: PSR B0329+54 & PSR B1642–03 – stars: magnetic field – radiation mechanisms: non-thermal

1 INTRODUCTION

Since the first pulsar is discovered in 1967 (Hewish et al. 1968), more than 2500 radio pulsars¹ (Manchester et al.

2005), and 200 gamma-ray pulsars² have been observed. A variety of models have been proposed to explain their radiation processes (Beskin et al. 2015). However, up to now, the pulsar radiation is still a question. Goldreich & Julian (1969) proposes that a rotating magnetic neutron star holds a charge-separated magnetosphere. Sturrock (1971)

* E-mail: gjn@pku.edu.cn

† E-mail: qjzhi@gznu.edu.cn

¹ <http://www.atnf.csiro.au/research/pulsar/psrcat/>

² <https://confluence.slac.stanford.edu/display/GLAMCOG/Public+List+of+>

quickly realized that a photon with energy larger than $2m_e c^2$ can generate electron-positron pairs to produce radio emission by the curvature radiation (CR). Subsequently, Ruderman & Sutherland (1975) develops Sturrock’s model. They propose the first accelerating model which is called “RS model”, which presents an accelerating regions (core gap model or CG model) above the polar cap of pulsar to accelerate the particles. These particles move out along the curved open magnetic field lines to produce radiation. The CG model is used widely in pulsar research.

In recent years, Qiao et al. (2004a) presents other accelerating region model, i.e., annular gap (AG) model, to understand the particles accelerating. Qiao et al. (2004a) suggests that there is an AG accelerating region above the polar cap of pulsars around the CG. The boundary of CG and AG is the critical field line (CFL) (Holloway 1975). In these two regions, the radio emission is believed to be generated by inverse Compton scattering (ICS) process between the secondary relativistic particles and low frequency waves (Qiao 1988a,b; Zhang & Qiao 1996; Qiao & Lin 1998). The ICS model can explain the pulse profiles with peaks number from one to five (Qiao & Lin 1998; Zhang et al. 2007), the widening or narrowing profiles with frequency increasing, the “mode changing” behavior (Qiao et al. 1996; Zhang et al. 1997a,b), and the polarization (Xu et al. 1997, 2000, 2001). Besides, this model combined with CG and AG can explain many observation phenomena at high energy bands (Qiao et al. 2004a; Lee et al. 2006a,b, 2009, 2010; Du et al. 2010, 2011, 2012, 2013, 2015).

Multi-band observation of pulsar is an effective tool for testing and constraining theoretical model. By analyzing the observed multi-frequency pulse profiles, the location, geometry, and spectrum of pulsar emission can be determined thus to constrain theoretical model. On the basis of the empirical classification for the observational properties of radio pulsars, (Rankin 1983, 1993) proposes that the radio beam consists of two hollow cones and a quasi-axial core normally. The debate between the “core-cone” beam models and other models (such as the “patchy” beam, fan-beam, microbeam pattern et al.) as well as multi-frequency observed data have been persisted by many authors (e.g. Lyne & Manchester 1988; Kramer et al. 1994; Manchester 1995; Gil & Krawczyk 1996; Melrose 1999; Mitra & Deshpande 1999; Gangadhara et al. 2001; Han & Manchester 2001; Kijak & Gil 2002; Manchester et al. 2005; Karastergiou & Johnston 2007; Maciesiak et al. 2011; Maciesiak & Gil 2011; Maciesiak et al. 2012; Beskin & Philippov 2012; Wang 2012; Fonseca et al. 2014; Wang et al. 2014; Cerutti et al. 2016; Dyks et al. 2016; Pierbattista et al. 2016; Teixeira et al. 2016). Besides, some theoretical perspectives (such as: the radio radiation beam is a hollow beam without a core cone; the pulse profiles at lower frequency are wider than those at higher frequencies) have been challenged by a large number of observations. The great variety of the pulse profiles as well as their frequency evolution indicate the high complexity of the pulsar beam patterns.

The multi-frequency pulse profiles characteristics of PSRs B0329+54 and B1642–03 challenge some theoretical models (e.g. the CR model). PSR B0329+54 is one of fairly bright pulsar in the northern sky. It has a spin

period of $P=0.715$ s (Hobbs et al. 2004). The pulse profiles of PSR B0329+54 have obvious central peak (Rankin 1983, 1993), and the form of mean pulse profiles shows five (Kramer 1994) or even nine components (Gangadhara et al. 2001; Gupta & Gangadhara 2003; Chen et al. 2011). The pulse profiles of this pulsar show narrower profiles at higher frequencies. PSR B1642–03 has a spin period of $P=0.388$ s (Manchester et al. 2005). The pulse profiles of PSR B1642–03 consists of a core and an inner cone component, and the pulse profiles at higher frequencies are wider than those at lower frequencies (Rankin 1983, 1993; Kramer 1994). These observed profiles properties of this two pulsars can hardly be understood in some theoretical models. Furthermore, as far as we know, no attempt has been made to understand a broad-band pulse profile evolution within the framework of most models. Therefore, it is of great significance to do more multi-band observations of pules profiles to test and constrain pulsar radiation mechanism model.

The major aim of this paper is to investigate the pulse profiles evolution over a two order of magnitude frequency range, and study the pulsar radio radiation model, particularly the ICS model. In § 2, we will present the observed data of these sources collected from the on-line database and the new observations by the Kunming 40 meters Telescope, Yunnan Astronomical Observatory, Chinese Academy of Sciences (CAS) and Tianma 65 meters Telescope, Shanghai Astronomical Observatory, CAS. In § 3, we separate the emission components of the integrated pulse profiles of PSRs B1642–03 and B0329+54 by the Gaussian fitting, calculate their radiation altitudes and present the radio radiation regions of these two sources. Conclusion and discussion are made in § 4.

2 OBSERVATION AND DATA REDUCTION

The multi-band pulse profiles are very important for the detailed study of the frequency evolution of pulse profiles. For PSR B0329+54, there are 10 profiles at frequencies 143, 408, 610, 925, 1642, 1410, 4750, 4850, 8500 and 10550 MHz (Pilia et al. 2015; Gould & Lyne 1998; von Hoensbroech & Xilouris 1997; Kramer 1994), while for PSR B1642–03, there are 8 profiles at frequencies 610, 925, 1408, 1410, 1642, 4850, 4750 and 10550 MHz (Seiradakis et al. 1995; von Hoensbroech & Xilouris 1997; Gould & Lyne 1998) are obtained from the European Pulsar Network database³. In order to provide more profiles to constraint theoretical model. We make observations at another three profiles at frequencies 2256, 5030 and 8600MHz. The pulse profiles at frequencies 5030 and 8600MHz are obtained from the observations with the Tianma 65 m Telescope, Shanghai Astronomical Observatory, CAS, at longitude $121^{\circ}.1$ E and latitude $+30^{\circ}.9$ N. The data were folded through Digital Backend System (Yan et al. 2015). The pulse profile at frequency 2256 MHz is obtained from the observation with the Kunming 40 m Telescope, Yunnan Astronomical Observatory, CAS, at longitude $102^{\circ}.8$ E and latitude $25^{\circ}.0$ N (Hao et al. 2010). The data was folded through

³ <http://www.epta.eu.org/epndb>

Table 1. Observational information

Center frequency (MHz)	Telescope	Bins	Bandwidth (MHz)	System temperature (K)	SEFD ^a (Jy)	Duration (s)
2256	Kunming 40 m ^(b)	512	251.5	80	350	13035.326
5030	Tianma 65 m ^(c)	1024	800	20	25	1773.823
8600	Tianma 65 m ^(c)	1024	800	35	50	3600

Note: ^a System Equivalent Flux Density; ^(b): (Hao et al. 2010); ^(c): (Yan et al. 2015).

Pulsar Digital Filter Bank 3 with parameters provided by PSRCAT⁴ (version 1.51) (Manchester et al. 2005). The radio-frequency interference (RFI) is removed manually with the software package PSRCHIVE⁵ (Hotan et al. 2004; van Straten et al. 2012). The observed information is listed in Table 1.

3 MULTI-BAND PROFILES ANALYSIS IN THE ICS MODEL

The beam shape and the acceleration regions are very important to constrain pulsar emission mechanisms. The emission beam contains two or three components, a center (core cone) and one or two nested cones (inner and outer cones). We obtain the pulse profile when the emission beam sweeps across the line of sight. The core, inner and outer cones components corresponds to the central peak and the peaks on the outside of pulse profiles, respectively. Each component of pulse profile is assumed to have a Gaussian shape and can be separated with Gaussian fitting (Wu et al. 1992; Kramer 1994; Wu et al. 1998). The cross section structure of the emission beam can be deduced by the average pulse profile (Oster & Sieber 1977; Rankin 1983; Manchester 1995; Qiao & Lin 1998; Han & Manchester 2001). In the magnetosphere of pulsar, the open field line region is divided into two parts by CFL. One part containing the magnetic axis is called the CG (Ruderman & Sutherland 1975) and the other part is the AG (Qiao et al. 2003a,b, 2004a, 2007). The locations and shapes of particle acceleration regions (CG and AG) above the polar cap can be determined by calculating the radiation altitude r (the distance from the pulsar center to the radiation point) of each component of pulse profile and the beaming angle θ_μ (the angle between the radiation direction and the magnetic axis).

3.1 Component-separation with Gaussian Fitting

Usually, the pulse profile is interpreted as the composition of different radiation components from different altitudes. Each component of the pulse profiles is assumed to have a Gauss shape and can be expressed by Gaussian functions. Here the multi-gaussian fitting method (Wu et al. 1992; Kramer 1994; Wu et al. 1998) is used to separate the different components of the pulse profiles. The Gaussian functions used in fitting can be written as:

$$y = \sum_{i=1}^N I_i \exp \left[-\frac{(x - p_i)^2}{2w_i^2} \right], \quad (1)$$

⁴ <http://www.atnf.csiro.au/research/pulsar/psrcat>

⁵ <http://psrchive.sourceforge.net>

where I_i , p_i and w_i are intensity, position of peak and standard deviation of i th Gaussian respectively. However, the residual exists between the results of model fitting and the observed data. In order to make the fitting results coincide better with the observed data, fitting parameters I_i , p_i and w_i . For a good fitting, the residual curve of the on-pulse part shall be noiselike, and as similar as possible to that of the off-pulse part. The final fitting parameters of various components of the pulse profiles of PSRs B0329+54 and B1642-03 are shown in Table 2 and 3, and the corresponding fitting curves are shown in Fig. 1 and 2. Besides, the evolution of pulse profiles versus frequencies are shown in Fig. 3.

For PSR B0329+54, the integrated profiles can be separated into five (Kramer 1994) or even nine components (Gangadhara et al. 2001). In this work, however, we fit each observational pulse profile with 5 Gaussian components. For PSR B1642-03, we fit each pulse profile with 3 Gaussian components to obtain satisfied residual. As the fitting results in Fig. 1-3, for PSR B0329+54 the integrated pulse profiles show narrower profiles at higher frequencies. Each integrated pulse profile of PSR B1642-03 has only a core and one inner cone component, and the pulse profiles at higher frequencies are wider than those at lower frequencies. These results coincide with the prediction by Qiao & Lin (1998); Qiao et al. (2001), i.e. the slow-rotation pulsars prefer to be “double-cones pulsars”, while the fast-rotation pulsars tend to show triple profiles.

3.2 Beam-frequency Evolution

We calculate geometrically the different radiation altitudes of components in various frequencies, and simulate the evolutions of radiation altitudes and beaming angles versus frequency in the ICS model. First, the magnetic field of pulsar is assumed to be dipole with the last open field line (LOF) tangent to the light cylinder (see (Zhang et al. 2007) for detailed equations). Secondly, the radiation is assumed to come from the open magnetic field line with the radiation direction tangent to that line. The radius of the magnetic field line where the radiation comes from is a specific times that of LOF. Thirdly, the radiation altitudes $r = \eta^{-2} R_e \sin^2 \theta$ of radiation components at a certain frequency can be determined with the parameters in Table 2-3 and the inclination angle α and the impact angle β in Fig. 4. R_e is the maximum radius of LOF. Obviously, for $\eta = 1$, the radiation is generated from LOF. θ is the polar angle between the magnetic axis and the radiation altitude r . In our calculation, the values of $\alpha = 30^\circ$ and $\beta = 2^\circ.1$ (Rankin 1993) for PSR B0329+54, and $\alpha = 68^\circ.2$, $\beta = 1^\circ.1$ (Lyne & Manchester 1988) for PSR B1642-03 are used respectively.

For the ICS process, the frequency ω' of the radiation photon (with the energy of $\hbar\omega'$) can be determined by the

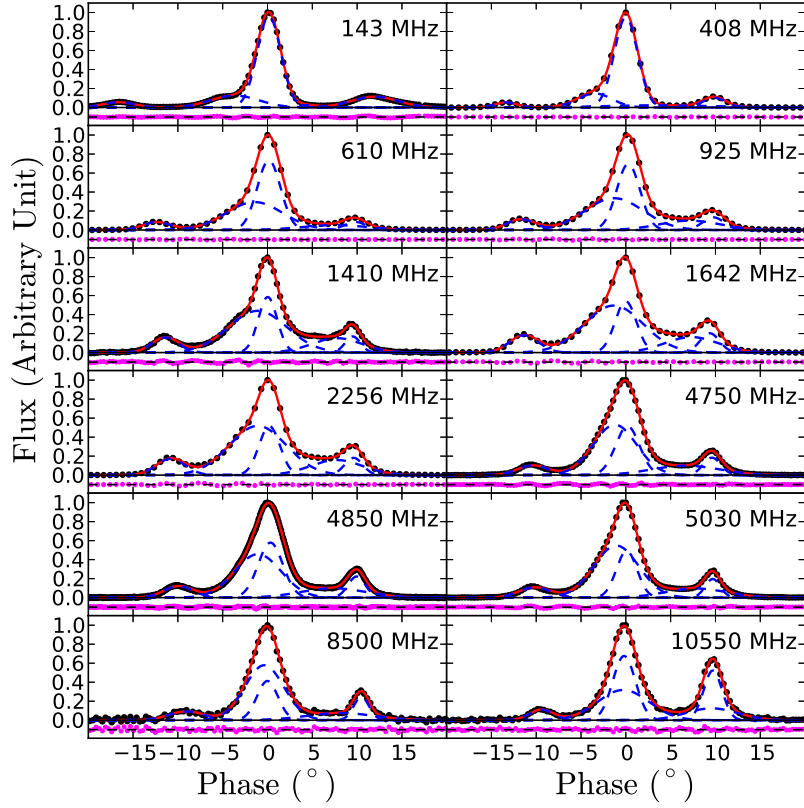


Figure 1. Gaussian fitting of PSR B0329+54 multi-frequency profiles in this figure. The black dots are the observation data. The red solid and blue dash lines are the fitting curves and single Gaussian respectively. The purplish red dots are the residuals. The maximum pulse flux is normalized, and the profiles are aligned at the position of central peak.

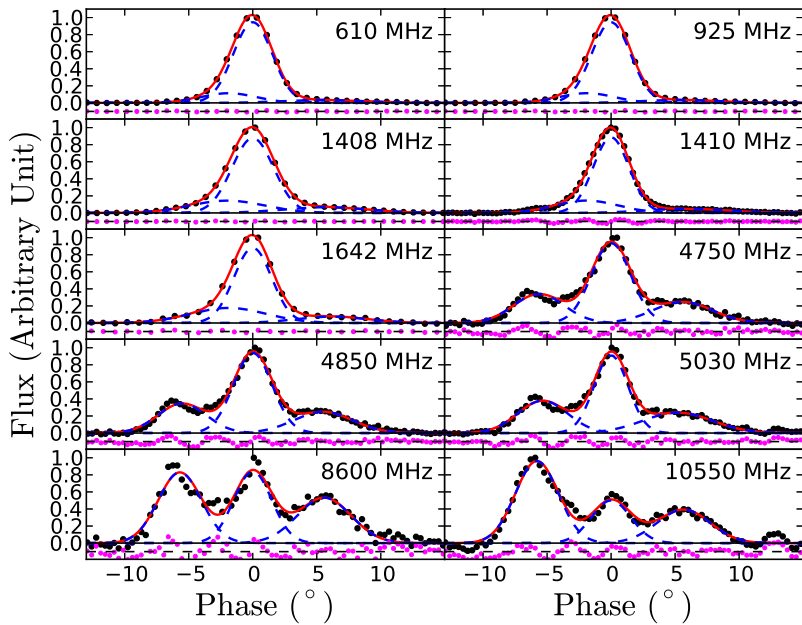


Figure 2. As Fig. 1, but for PSR B1642-03.

Table 2. The Gaussian fitting parameters of PSR B0329+54.

f (MHz)	i	p_i	I_i	w_i	f (MHz)	i	p_i	I_i	w_i
143	1	-16.767±0.07	0.056±0.002	1.766± 0.07	2256	1	-11.007±0.05	0.173±0.004	1.604±0.05
	2	-3.838±0.19	0.126±0.003	2.667± 0.13		2	-1.298±0.15	0.518±0.02	3.188±0.07
	3	0.0	0.96±0.01	1.322± 0.01		3	0.0	0.516±0.02	1.162±0.03
	4	4.208±0.17	0.024±0.003	1.126± 0.19		4	7.492±0.44	0.159±0.01	2.896±0.26
	5	11.769±0.05	0.114±0.002	2.604± 0.05		5	9.401±0.05	0.182±0.02	1.006±0.07
408	1	-13.397±0.03	0.053±0.001	1.262± 0.03	4750	1	-10.542±0.05	0.103±0.003	1.708±0.05
	2	-3.47±0.06	0.148±0.003	1.906± 0.05		2	-1.409±0.18	0.531±0.04	2.423±0.06
	3	0.0	0.951±0.004	1.299±0.004		3	0.0	0.514±0.04	1.341±0.04
	4	3.395±0.62	0.023±0.001	5.788± 0.31		4	6.481±0.73	0.099±0.003	3.754±0.41
	5	9.847±0.02	0.101±0.001	1.27±0.021		5	9.423±0.03	0.183±0.01	0.988±0.04
610	1	-12.53±0.03	0.084±0.001	1.57± 0.03	4850	1	-10.25±0.02	0.121±0.001	1.629±0.02
	2	-1.602±0.17	0.295±0.01	3.169± 0.07		2	-1.403±0.07	0.458±0.01	2.586±0.02
	3	0.0	0.733±0.01	1.308± 0.01		3	0.0	0.579±0.01	1.372±0.01
	4	7.377±0.98	0.052±0.003	3.651± 0.58		4	6.987±0.24	0.099±0.001	3.6±0.15
	5	9.606±0.04	0.086±0.01	1.209± 0.07		5	9.617±0.01	0.223±0.003	0.959±0.01
925	1	-11.966±0.04	0.114±0.002	1.581± 0.04	5030	1	-10.262±0.05	0.109±0.002	1.768±0.05
	2	-1.586±0.33	0.335±0.02	3.267± 0.14		2	-1.156±0.06	0.548±0.01	2.505±0.03
	3	0.0	0.695±0.02	1.301± 0.02		3	0.0	0.492±0.01	1.149±0.02
	4	6.84±1.06	0.099±0.01	3.37± 0.50		4	7.734±0.26	0.097±0.004	3.35±0.20
	5	9.486±0.04	0.134±0.01	1.208± 0.07		5	9.6±0.02	0.196±0.01	0.847±0.03
1410	1	-11.427±0.04	0.159±0.004	1.479± 0.04	8500	1	-9.037±0.16	0.093±0.01	1.942±0.18
	2	-1.123±0.09	0.439±0.01	3.281± 0.05		2	-0.352±0.08	0.578±0.09	2.184±0.12
	3	0.0	0.585±0.01	1.055± 0.02		3	0.0	0.413±0.09	1.167±0.10
	4	7.719±0.23	0.152±0.01	2.751± 0.15		4	8.132±0.74	0.076±0.01	3.717±0.58
	5	9.482±0.03	0.17±0.01	0.847± 0.05		5	10.483±0.04	0.244±0.01	0.858±0.05
1642	1	-11.365±0.04	0.182±0.004	1.596± 0.04	10550	1	-9.255±0.08	0.111±0.01	1.338±0.08
	2	-1.326±0.18	0.495±0.02	3.291± 0.09		2	-0.098±0.07	0.318±0.04	2.861±0.16
	3	0.0	0.541±0.02	1.18± 0.03		3	0.0	0.676±0.04	1.273±0.04
	4	7.338±0.52	0.163±0.01	2.962± 0.29		4	9.765±0.18	0.125±0.02	2.86±0.28
	5	9.375±0.04	0.204±0.02	1.08± 0.07		5	9.899±0.02	0.522±0.02	1.035±0.03

Note: f is the observed frequency, I_i , p_i , w_i are the intensity, peak position, standard deviation of the i th Gaussian component, respectively.

Table 3. The Gaussian fitting parameters of PSR B1643–03.

f (MHz)	i	p_i	I_i	w_i	f (MHz)	i	p_i	I_i	w_i
610	1	-1.895±2.52	0.114±0.12	2.136±0.73	4750	1	-5.641±0.08	0.34±0.01	1.973±0.09
	2	0.0	0.946±0.17	1.523±0.05		2	0.0	0.937±0.01	1.529±0.04
	3	5.427±0.76	0.034±0.003	3.069±0.48		3	5.589±0.15	0.247±0.01	2.314±0.15
925	1	-1.894±2.35	0.114±0.11	2.136±0.68	4850	1	-5.526±0.07	0.346±0.01	1.877±0.07
	2	0.0	0.946±0.16	1.523±0.05		2	0.0	0.939±0.01	1.506±0.03
	3	5.427±0.71	0.034±0.003	3.069±0.45		3	5.497±0.12	0.25±0.01	2.281±0.13
1408	1	-1.991±0.76	0.144±0.03	2.886±0.25	5030	1	-5.344±0.07	0.38±0.01	1.942±0.08
	2	0.0	0.877±0.04	1.619±0.02		2	0.0	0.912±0.02	1.329±0.03
	3	5.664±0.65	0.067±0.01	3.249±0.31		3	5.202±0.20	0.239±0.01	2.709±0.20
1410	1	-1.908±0.99	0.145±0.04	2.437±0.33	8600	1	-5.697±0.08	0.829±0.03	1.693±0.08
	2	0.0	0.886±0.07	1.397±0.04		2	0.0	0.839±0.03	1.482±0.10
	3	5.914±0.88	0.048±0.004	3.191±0.57		3	5.578±0.16	0.533±0.03	2.102±0.17
1642	1	-1.896±1.18	0.177±0.05	2.959±0.43	10550	1	-5.798±0.06	0.961±0.03	1.676±0.07
	2	0.0	0.881±0.07	1.471±0.05		2	0.0	0.5±0.03	1.542±0.16
	3	6.201±1.06	0.074±0.01	2.778±0.61		3	5.665±0.20	0.393±0.02	2.069±0.21

Note: with the same parameters as Table 2

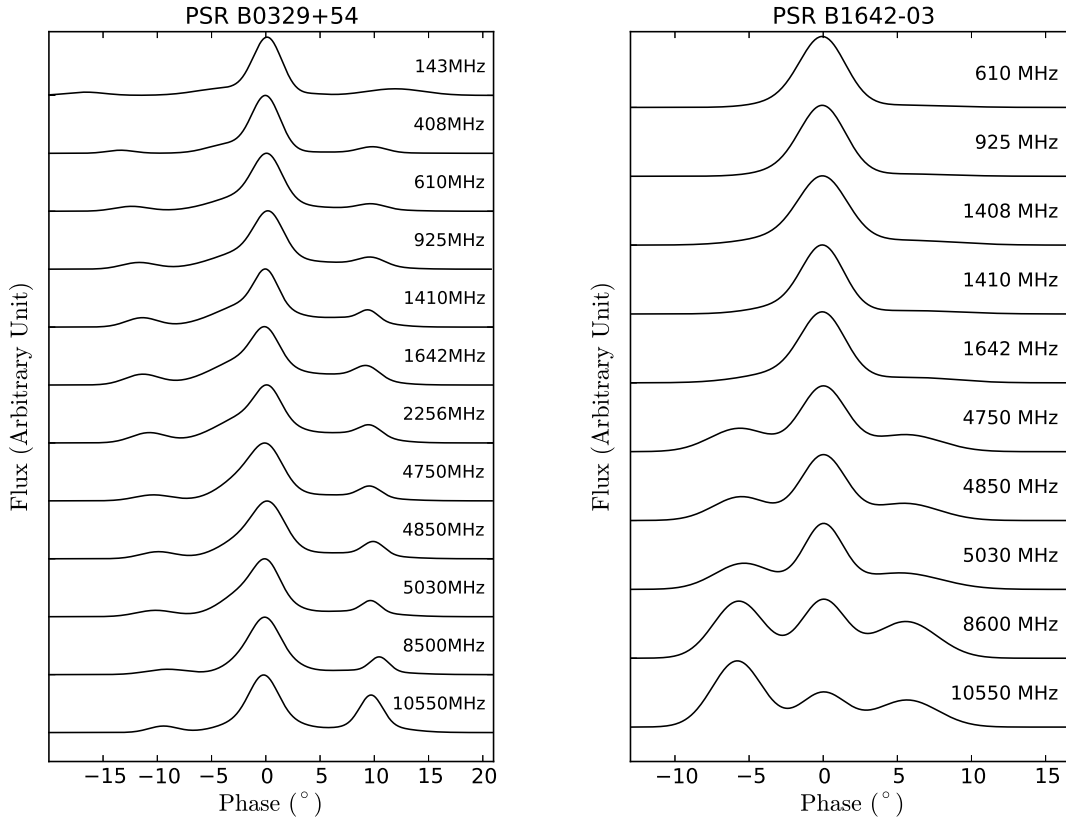


Figure 3. The fitting curves evolution versus the observing frequency.

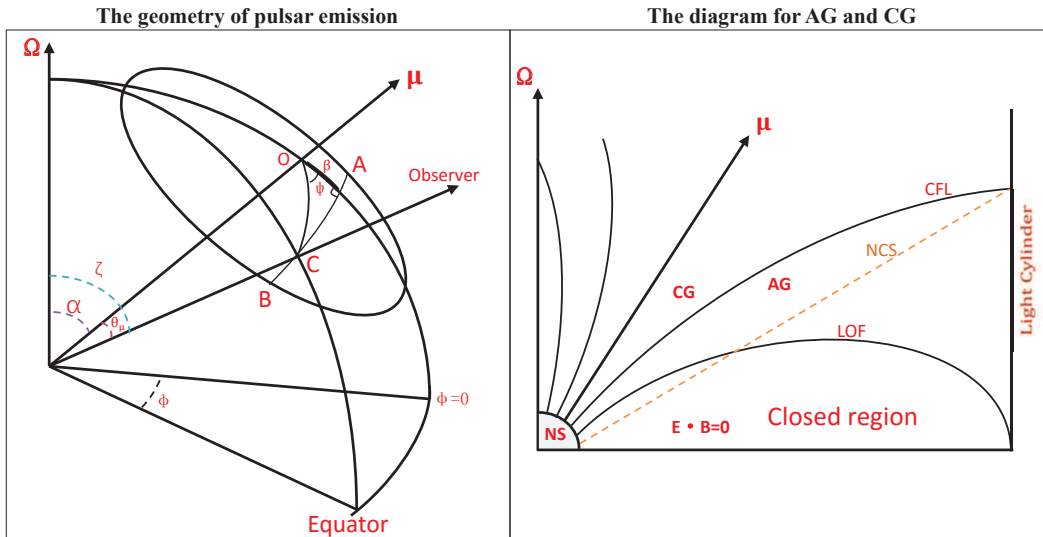


Figure 4. Left: the geometry of pulsar emission (Zhang et al. 2007). Ω and μ are the rotation axis and the magnetic axis. ζ , α , $\beta = \zeta - \alpha$ and θ_μ are the angle of the observer's line of sight to the rotation axis, the magnetic inclination angle, the impact angle and the angle of radiation direction to the magnetic axis, respectively. ϕ represents the azimuth angle around the rotation axis, ψ is the angle between the magnetic field plane and the Ω - μ plane. C is a point that we observe the radiation when the line of sight sweeps the emission beam from A to B . Right: a simple diagram for the AG and the CG in the magnetosphere of neutron star (NS) (Qiao et al. 2007). “NCS” represents the null change surface where $\Omega \cdot B = 0$. “CFL” and “LOF” are the CFL and the last open field line respectively.

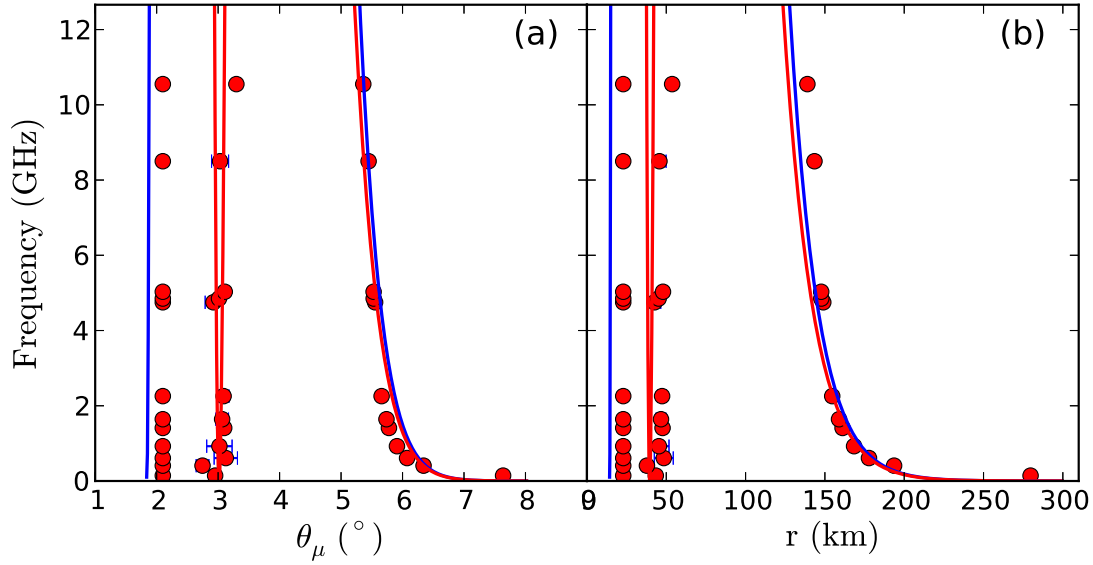


Figure 5. The simulating results of beam-frequency evolution of PSR B0329+54 in the ICS model. The figure (a) and (b) present the evolutions of beaming angle θ_μ and the emission altitudes versus frequency respectively. The red dots are the emission altitudes. The blue and red solid lines are the ICS fitting curves. The values of γ_0 and k are set to 2×10^5 and 0.329 respectively.

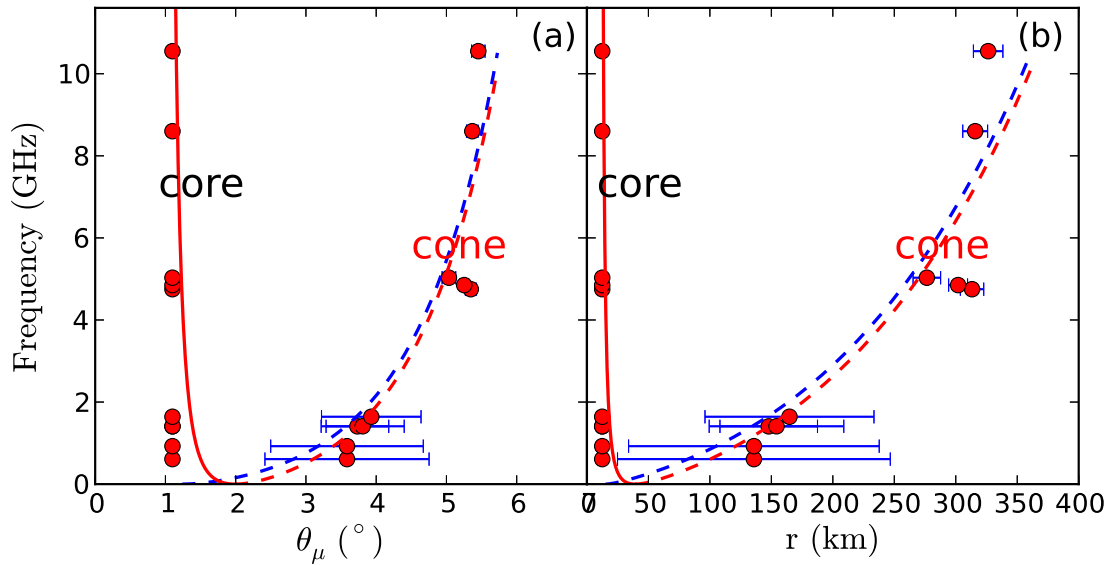


Figure 6. As Fig. 5, but for PSR B1642-03. $\gamma_0 = 1.6 \times 10^3$, $k = -0.02$. The fitting curves are plotted with solid curves for core component and dashed curves for cone component.

following equation (see Qiao & Lin 1998):

$$\omega' = 2\gamma^2\omega_0(1 - \eta \cos \theta_i), \quad (2)$$

where θ_i is the angle between the outgoing direction (initial direction of photons moving from the sparking point, see sparking point A in Fig.1 in Qiao & Lin 1998) and incoming direction (radiation direction) of photons; $\omega_0 = 2\pi \times 10^6$ rad/s (Lu et al. 2016) is the initial angular frequency of the low frequency wave; γ is the Lorentz factor of particle with the value $\gg 1$; $\eta = \frac{v}{c} \approx 1$. θ_i can be deter-

mined by the following equation (Qiao & Lin 1998):

$$\cos \theta_i = \frac{2 \cos \theta + (1 - 3\cos^2 \theta) \frac{R}{r}}{(1 + 3\cos^2 \theta)^{1/2} (1 - 2\frac{R}{r} \cos \theta + \frac{R}{r})}, \quad (3)$$

where R is the radius of pulsar. In our calculation, we consider a case that the low frequency wave is produced by the electron oscillating at the sparking points A or A' (see Fig. 7) in the gap. The high energy particles will lose energy owing to be scattered by the thermal photons and low frequency waves when the particles move along with the field

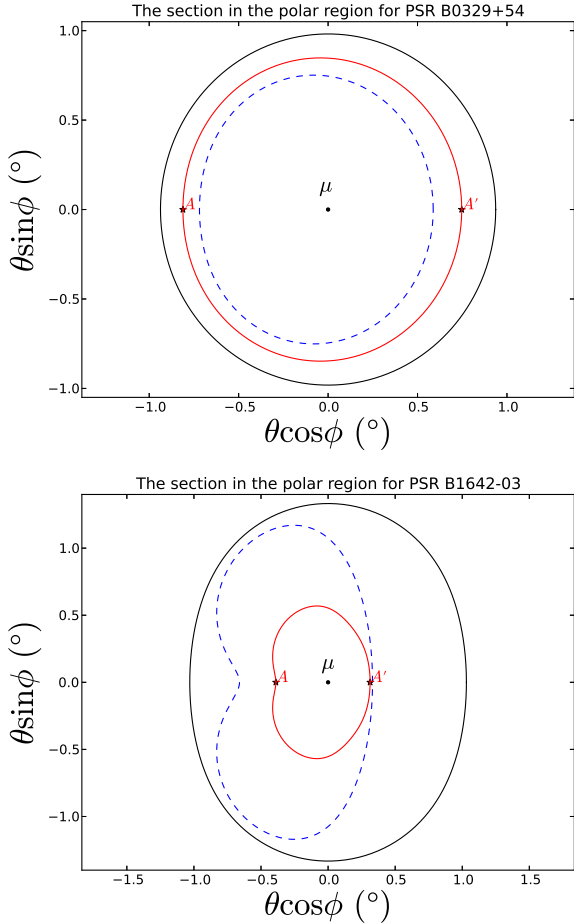


Figure 7. The black solid and blue dashed lines are the LOF and CFL respectively. The region between blue dashed line and black solid line is AG, the region surrounded by blue dashed line is the CG. The red solid line is the magnetic field line where the radiation comes from. The red solid line is also the section of all the sparking points in the AG or the CG. The red star dots A and A' are the sparking points used in our calculation. For PSRs B0329+54 and B1642–03, the values of α are $30^\circ.0$ and $68^\circ.2$ respectively.

lines. The lorentz factor of the particle is assumed to vary with the exponential form: $\gamma = \gamma_0 \exp(-k \frac{r-R}{R})$, where γ_0 is the initial lorentz factor, k is a factor for the energy loss of particles. The locations of the sparking points and the values of γ_0 and k can be obtained by the ICS model simulating the evolutions of radiation altitudes and beaming angles versus the radiation frequency.

The simulative results of the ICS model are shown in Fig. 5 (PSR B0329+54) and Fig. 6 (PSR B1642–03), where the red and blue solid (dashed) lines represent the theoretical curves of ICS model that the observed waves outgoing from the points A and A' (see Fig. 7), respectively. Fig. 5(a) and Fig. 6(a) present the beaming angle evolves with the radiation frequency. While Fig. 5(b) and Fig. 6(b) show the radiation altitude evolves with the radiation frequency. By the ICS model simulating the evolutions of radiation altitude and beaming angle versus the radiation frequency, the parameter values of $\gamma_0 \sim 2 \times 10^5$ and $k \sim 0.329$ for PSR B0329+54, and $\gamma_0 \sim 1.6 \times 10^3$ and $k \sim -0.02$ for

PSR B1642–03 are obtained, respectively. Meanwhile, the field lines where the radiation comes from and the sparking points A and A' are also determined by the simulation. The foots of the field lines above the polar cap are located at $0.98 R_p$ for PSR B0329+54 and $0.46 R_p$ for PSR B1642–03 respectively. The locations of sparking points above the polar cap are $0.98 R_p$ for PSR B0329+54 and $0.46 R_p$ for PSR B1642–03 respectively, where $R_p = R^{1.5} \Omega^{0.5} c^{-0.5}$ represents the polar cap radius is defined by the foot of LOF (R , Ω and c are the pulsar radius, rotation angular velocity and light speed, respectively Ruderman & Sutherland 1975). In Fig. 5–6, the theoretical curve of the ICS model shows a “down-up-downward” trend, which is consistent with the conclusion of (Qiao & Lin 1998; Zhang et al. 2007). For each profile, the radiation altitudes of the inner cone components are lower than those of the outer cone components. The radiation altitudes of the outer components decrease with the radiation frequency increasing. While, the radiation altitudes of inner cone components increase with the frequency increasing.

3.3 Radiation Region

In an oblique rotator with a dipolar magnetic field, the shape of gap is a function of the pulsar period and inclination angle α (Qiao et al. 2004a; Wang et al. 2006; Lee et al. 2006a). The CG and AG in the open magnetic field region are shown in Fig. 4. Qiao et al. 2004a points out that the sparking may take place in these two gaps, which will lead to pairs production and generate the secondary particles. These particles would be accelerated in the CG or AG to produce radiation through the ICS process. The radiation region of the pulsar can be determined conclusively if the sparking point and the magnetic field line where the radiation comes from are determined (the detailed calculation methods are given by Qiao et al. (2004a); Wang et al. (2006); Lee et al. (2006a)).

We try to determine the radio radiation regions of PSRs B0329+54 and B1642–03 by using the simulative results in §3.2. The shapes and widths of the radiation regions above the polar cap are shown in Fig. 7. For PSR B0329+54, the section (the red solid line) of the foots of field lines where the radiation comes from and the sparking points A and A' above the polar cap are located at the region between those of the LOF (the black solid line) and CFL (the blue dashed line). We also obtain a simulation of beam-frequency, though the simulation is not optimal considering this case that the radiation is generated from the CG. Therefore, the CG and AG can be responsible for the radiation of PSR B0329+54. For PSR B1642–03, however, the section (the red solid line) of the foots of field lines where the radiation comes from and the sparking points above the polar cap are located at the region surrounded by the CFL, which means that the radiation of PSR B1642–03 is generated mainly from the CG.

4 CONCLUSIONS AND DISCUSSIONS

With the multi-Gaussian function, we separate the radiation components of the multi-band radio pulse profiles of PSRs

B0329+54 and B1642–03, and calculate the radiation altitude of each radiation component ($r = 20 \sim 280$ km for PSR B0329+54 and $r = 10 \sim 330$ km for PSR B1642–03). Then we simulate further the evolutions of radiation altitudes and beaming angles with the ICS model and obtain the Lorentz factors ($\gamma_0 \simeq 10^5$ for PSR B0329+54 and $\gamma_0 \simeq 10^3$ for PSR B1642–03) and energy loss factors of high energy particles ($k = 0.329$ for PSR B0329+54 and $k = -0.02$ for PSR B1642–03). Finally, we get the radio radiation regions of the two sources.

- (1) It is suspected that the radio emission beam of pulsars may include core and multi-cone components (Rankin 1983, 1993; Lyne & Manchester 1988; Wu et al. 1992, 1998; Manchester 1995; Zhang et al. 2007). Now, the pulse profiles of PSRs B0329+54 and B1642–03 show obvious multi-peak, which can be described by multi-Gaussian functions (5 Gaussians for PSR B0329+54 and 3 Gaussians for PSR B1642–03, see Fig.1 and Fig.2 for details), which supports the scenario of core and cone components. However, the formation and radiation mechanism of multi-components are still disputable. We find that the multi-components of the two sources can be described well by the ICS model, which implies that the core and cones components may be generated by the same radiation mechanism. This is consistent with the conclusion of Lyne & Manchester (1988).
- (2) In most cases the integrated pulse profiles of pulsars are extremely stable. However, in case of a moding pulsar (Backer 1970; Helfand et al. 1975; Wang et al. 2007; Kijak et al. 1998; van Leeuwen et al. 2002; Redman et al. 2005), during an observation, if a mode change occurs, the observed profile will be different from the profile of any individual mode. Furthermore, when moding occurs, the observed pulse profile will be no longer stable because the relative contribution of each mode is different. For PSR 0329+54, the mode switching of the pulse profile is observed (Lyne et al. 1971; Bartel et al. 1982; Hesse et al. 1973; Izvekova et al. 1994; Kuz'min & Izvekova 1996; Suleimanova et al. 2002; Chen et al. 2011). Does this mode changing influence our results? Kuz'min & Izvekova (1996) found that for PSR 0329+54, "When the mode changes, the component structure (the number of the components and their positions in phase) does not change; only the relative intensity of the components varies". We also get the same conclusion by analyzing some mode changing data of PSR B0329+54. Therefore the mode switching phenomenon does not influence our result. In future, we plan to use large-aperture telescopes (e.g., FAST) for long-term monitoring of some pulsars including these two pulsars and study the pulse profiles evolution with the new data and the ICS model thus to verify the conclusions presented in this paper.
- (3) It is very important to determine the radiation locations by analyzing the observed multi-frequency pulse profiles for understanding how the radiation is generated in pulsar magnetosphere and constraining the pulsar radiation models. For PSRs B0329+54 and B1642–03, the sparking and related radiation can take place in both CG and AG. Can we observe the radiation of

these two pulsars from both of CG and AG? The answer depends on the inclination angle α and the impact angle β (or viewing angle $\zeta = \alpha + \beta$). From the observed values of α and β (Lyne & Manchester 1988; Rankin 1993), under the dipole magnetic field assumption, radiation regions are calculated geometrically. It is found that the CG or AG can be responsible for the radio radiation of PSR B0329+54. Whereas, the radiation is likely to be generated just in the CG for PSR B1642–03. Besides the particle acceleration and radiation locations, another question is: what shapes of pulse profiles can be observed? The shapes of pulse profiles change with frequencies. The beam-frequency evolution presents a constraint to all theoretical models. The ICS model has two typical "beam-frequency map" (The observing frequency is plotted versus the beaming angle or altitudes of radiation points) (Qiao & Lin 1998; Qiao et al. 2001). The "beam-frequency map" of PSRs B0329+54 and B1642–03 (Fig. 5 and Fig. 6 in this paper) show these two types respectively. Especially the "beam-frequency map" of PSR B1642–03 shows that the pulse profiles become wider at higher frequencies, which challenges other theoretical models.

- (4) The Lorentz factors we used for simulating the observed data are $\sim 10^5$ for PSR B0329+54, and $\sim 10^3$ for PSR B1642–03 (see Fig.5 and Fig.6). These Lorentz factors are larger than those ($\gamma \simeq 800$) of secondary particles and lower than the energy of the primary particles $\gamma_0 \simeq 10^6$ given by Ruderman & Sutherland (1975). In the CR model (Ruderman & Sutherland 1975), pair production needs the Lorentz factors of primary particles as large as 10^6 . As discussed by Zhang et al. (2007), not all pairs are produced at the bottom of the gap, therefore not all primary particles can gain such a large Lorentz factor. When the pairs are generated outside the gap, the Lorentz factor shall be $\lesssim 10^6$. This means the Lorentz factor γ_0 used in this paper is reasonable.

ACKNOWLEDGEMENTS

This work was supported by the National Basic Research Program of China (Grant No.2012CB821800), the International Partnership Program, the Strategic Priority Research Program and the Strategic Priority Research Program "The Emergence of Cosmological Structures" of CAS (Grant Nos.114A11KYSB20160008, XDB23000000 and XDB09000000), the NSFC (Grant Nos. 11565010, 11373011, 11225314, 11033008, 11165005, 11173046, 11403073, 11303069, 11173041), the science and technology innovation talent team (Grant No. (2015)4015), the Training Program for Excellent Young Talents (Grant No. 2011-29), the High level Creative Talents (Grant No.(2016)-4008) and the Innovation Team Foundation of the Education Department (Grant No. [2014]35) of Guizhou Province, the Natural Science Foundation of Shanghai No. 13ZR1464500, the Scientific Program of Shanghai Municipality (08DZ1160100), the Knowledge Innovation Program of CAS (grant No. KJCX1-YW-18), the Strategic Priority Research Program The Emergence of Cosmological Structures of CAS (grant No. XDB09000000), Doctoral Starting up Foundation of Guizhou Normal University 2014, Science

and Technology Foundation of Guizhou Province (Grant Nos. J[2015]2113 and LH[2016]7226) and the Postgraduate Innovation Foundation of Guizhou normal university (Grant No. 201527). This work is also supported partially by the fund of “Special Demonstration of Space Science”.

We would like to thank the Yunnan Astronomical Observatory, CAS & Shanghai Astronomical Observatory, CAS, and the European pulsar network database for providing observation condition and valuable data resources.

REFERENCES

- Bartel N., Morris D., Sieber W., et al., 1982, *ApJ*, 258, 776
- Backer D. C. 1970, *Nature*, 228, 42
- Beskin V. S., Chernov S. V., Gwinn C. R., & Tchekhovskoy A. A. 2015, *Space Sci. Rev.*, 191, 207
- Beskin V. S., & Philippov A. A., 2012, *MNRAS*, 425, 814
- Cerutti B., Philippov A. A., & Spitkovsky A., 2016, *MNRAS*, 457, 2401
- Chen J. L., Wang H. G., Wang N., et al., 2011, *ApJ*, 741, 48
- Du Y. J., Qiao G. J., Han J. L., et al., 2010, *MNRAS*, 406, 2671
- Du Y. J., Han J. L., Qiao G. J., et al., 2011, *ApJ*, 731, 2
- Du Y. J., Qiao G. J., & Wang W., 2012, *ApJ*, 748, 84
- Du Y. J., Qiao G. J., & Chen D., 2013, *ApJ*, 763, 29
- Du Y., Qiao G., Shuai P., et al., 2015, *ApJ*, 801, 131
- Dyks J., Serylak M., Osłowski S., et al. 2016, *A&A*, 593, A83
- Fonseca N. N. J., Alencar S. H. P., Bouvier J., et al., 2014, *A&A*, 567, A39
- Gangadhara R. T., & Gupta Y., 2001, *ApJ*, 555, 31
- Gil J., & Krawczyk A., 1996, *IAU Colloq. 160: Pulsars: Problems and Progress*, 105, 213
- Goldreich P., & Julian W. H., 1969, *ApJ*, 157, 869
- Gould D. M., & Lyne A. G., 1998, *MNRAS*, 301, 235
- Gupta Y., & Gangadhara R. T., 2003, *ApJ*, 584, 418
- Han J. L., Manchester R. N., 2001, *MNRAS*, 320, L35
- Hao L. F., Wang M., & Yang J., 2010, *Research in Astronomy and Astrophysics*, 10, 805
- Helfand D. J., Manchester R. N., & Taylor J. H., 1975, *ApJ*, 198, 661
- Hesse K. H., Sieber W., & Wielebinski R., 1973, *Nature Physical Science*, 245, 57
- Hewish A., Bell S. J., Pilkington J. D. H., et al., 1968, *Nature*, 217, 709
- Holloway N. J., 1975, *MNRAS*, 171, 619
- Hobbs G., Lyne A. G., Kramer M., et al., 2004, *MNRAS*, 353, 1311
- Hotan A. W., van Straten W., & Manchester R. N., 2004, *Publ. Astron. Soc. Australia*, 21, 302
- Izvekova V. A., Jessner A., Kuzmin A. D., et al., 1994, *A&AS*, 105
- Karastergiou A., & Johnston S., 2007, *MNRAS*, 380, 1678
- Kijak J., Kramer M., Wielebinski R., et al., 1998, *A&AS*, 127, 153
- Kijak J., & Gil J., 2002, *A&A*, 392, 189
- Kramer M., 1994, *A&AS*, 107, 527
- Kramer M., Wielebinski R., Jessner A., et al., 1994, *A&AS*, 107, 394
- Kuzmin A. D., & Izvekova V. A., 1996, *Astronomy Letters*, 22, 394
- Lee K. J., Qiao G. J., Wang H. G., et al., 2006a, *Advances in Space Research*, 37, 1988
- Lee K. J., Qiao G. J., Wang H. G., et al., 2006b, *Chinese Journal of Astronomy and Astrophysics Supplement*, 6, 120
- Lee K. J., Cui X. H., Wang H. G., et al., 2009, *ApJ*, 703, 507
- Lee K. J., Du Y. J., Wang H. G., et al., 2010, *MNRAS*, 405, 2103L
- Lu J. G., Du Y. J., Hao L. F., et al., 2016, *ApJ*, 816, 76
- Lyne A. G., Smith F. G., & Graham D. A., 1971, *MNRAS*, 153, 337
- Lyne A. G., & Manchester R. N., 1988, *MNRAS*, 234, 477
- Maciesiak K., Gil J., & Ribeiro V. A. R. M., 2011, *MNRAS*, 414, 1314
- Maciesiak K., & Gil J., 2011, *MNRAS*, 417, 1444
- Maciesiak K., Gil J., & Melikidze G., 2012, *MNRAS*, 424, 1762
- Mitra D., & Deshpande A. A., 1999, *A&A*, 346, 906
- Manchester R. N., 1995, *Journal of Astrophysics and Astronomy*, 16, 107
- Manchester R. N., Hobbs G. B., Teoh A., et al., 2005, *AJ*, 129, 1993
- Melrose D. B., & Gedalin M. E., 1999, *ApJ*, 521, 351
- Oster L., & Sieber W., 1977, *A&A*, 58, 303
- Pierbattista M., Harding A. K., Gonthier P. L., et al., 2016, *A&A*, 588, A137
- Pilia M., Trois A., Pellizzoni A. P., et al., 2015, *arXiv:1512.01361*
- Qiao G. J., 1988a, *Vistas in Astronomy*, 31, 393
- Qiao G. J., 1988b, *Supernovae, Remnants, Active Galaxies, Cosmology*, 88
- Qiao G. J., & Lin W. P., 1998, *A&A*, 333, 172
- Qiao G. J., Liu J. F., Zhang B., et al., 2001, *A&A*, 377, 964
- Qiao G. J., Lee K. J., Wang H. G., et al., 2003a, in *IAU Symp. 214, High Energy Processes and Phenomena in Astrophysics*, ed. X. D. Li, V. Trimble, & Z. R. Wang (San Francisco: ASP), 167
- Qiao G. J., Lee K. J., Wang H. G., et al., 2003b, in *ASP Conf. Ser. 302, Radio Pulsars*, ed. M. Bailes, D. J. Nice, & S. E. Thorsett (San Francisco: ASP), 83
- Qiao G. J., Lee K. J., Wang H. G., et al., 2004a, *ApJ*, 606, L49
- Qiao G. J., Lee K. J., Zhang B., et al., 2007, *Chinese J. Astron. Astrophys.*, 7, 496
- Qiao G. J., & Zhang B., 1996, *A&A*, 306, L5
- Rankin J. M., 1983, *ApJ*, 274, 333
- Rankin J. M., 1993, *ApJS*, 85, 145
- Redman S. L., Wright G. A. E., & Rankin J. M., 2005, *MNRAS*, 357, 859
- Ruderman M. A., & Sutherland P. G., 1975, *ApJ*, 196, 51
- Seiradakis J. H., Gil J. A., Graham D. A., et al., 1995, *A&AS*, 111, 205
- Sturrock P. A. 1971, *ApJ*, 164, 529
- Suleimanova S. A., & Pugachev V. D., 2002, *Astron. Rep.*, 46, 34
- Teixeira M. M., Rankin J. M., Wright G. A. E., et al., 2016, *MNRAS*, 455, 3201
- von Hoensbroech A., & Xilouris K. M., 1997, *A&AS*, 126
- van Straten W., Demorest P., & Osłowski S., 2012, *Astronomical Research and Technology*, 9, 237
- van Leeuwen A. G. J., Kouwenhoven M. L. A., Ramachandran R., et al., 2002, *A&A*, 387, 169
- Wang N., Manchester R. N., & Johnston S., 2007, *MNRAS*, 377, 1383
- Wang P. F., Wang C., & Han J. L., 2012, *MNRAS*, 423, 2464
- Wang H. G., Qiao G. J., Xu R. X., et al., 2006, *MNRAS* 366, 945
- Wang H. G., Pi F. P., Zheng, X. P., et al., 2014, *ApJ*, 789, 73
- Wu X. J. et al., 1992, *IAU Coll.*, 128172
- Wu X. J., Gao X. Y., Rankin J. M. et al., 1998, *ApJ*, 116, 1984
- Xu R. X., Qiao G. J., & Han J. L., 1997, *A&A*, 323, 395
- Xu R. X., Liu J. F., Han J. L., et al., 2000, *ApJ*, 535, 354
- Xu R., Qiao G., & Han J., 2001, *Progress in Astronomy*, 19, 267
- Yan Z., Shen Z. Q., Wu X. J., et al., 2015, *ApJ*, 814, 5
- Zhang B., & Qiao G. J., 1996, *A&A*, 310, 135
- Zhang B., Qiao G. J., & Han J. L., 1997, *ApJ*, 491, 891
- Zhang B., Qiao G. J., Lin W. P., et al., 1997, *ApJ*, 478, 313
- Zhang H., Qiao G. J., Han J. L., et al., 2007, *A&A*, 465, 525

This paper has been typeset from a $\text{\TeX}/\text{\LaTeX}$ file prepared by the author.